



Original Paper

Cavitation cloud impingement and scattering motion of jet in rock breaking process

Qi-Heng Zhu^a, Fei Ma^{a, b}, Bo-Shen Liu^{a, *}, Tian-Xu Luo^b, Yan Pan^a^a School of Mechanical Engineering, University of Science and Technology Beijing, Beijing, 100083, China^b Shunde Innovation School, University of Science and Technology Beijing, Shunde, 528339, Guangdong, China

ARTICLE INFO

Article history:

Received 15 November 2023

Received in revised form

21 May 2024

Accepted 21 May 2024

Available online 23 May 2024

Edited by Jia-Jia Fei

Keywords:

Erosion

Cavitating jet

Rock breaking

Flow visualization

3D-printing

ABSTRACT

The cavitation cloud impingement of the jet in the rock breaking process was experimentally investigated to reveal the jet erosion mechanism in drilling of petroleum exploitation. Serial erosion tests and flow visualization were performed, where the cavitation cloud motion in the erosion crater was obtained with the designed transparent specimen. Various erosion patterns were identified in the whole erosion process based on the eroded specimen topography. The shallow eroded crater with a shrinking erosion area is generated by the combination of impinging and scattering cavitation clouds. The increase of l_d promotes the development of cavitation cloud σ_c but reduces the impingement frequency f_d , suggesting that the jet aggressive ability is enhanced when the balance between σ_c and f_d is reached. The cavitation cloud motion in the erosion crater was investigated with the transparent specimen. The erosion in the crater at shorter exposure periods T_e is generated by the combination of impingement and restricted scattering of cavitation clouds. With the continuous development of the erosion damage, the jet's aggressive ability is diminished due to the erosion expansion on sandstone, where the cavitation clouds impinge on the target and then collapse and vanish without restricted scattering.

© 2024 The Authors. Publishing services by Elsevier B.V. on behalf of KeAi Communications Co. Ltd. This is an open access article under the CC BY-NC-ND license (<http://creativecommons.org/licenses/by-nc-nd/4.0/>).

1. Introduction

As a high-efficiency rock breaking method in the ambient pressure condition, the cavitating jet has great potential in many underground engineering fields including petroleum exploitation (Li et al., 2010; Liu et al., 2022; Jiang et al., 2022) and coal mining (Lu et al., 2017; Ge et al., 2022). The cavitation clouds periodically shed, flow and impinge on the downstream rock surface, where the erosion damage in rock breaking is primarily induced by the cumulative highspeed micro-jet impingement of bubble collapse (Liu et al., 2022).

The aggressive ability of the cavitating jet in rock breaking significantly influences drilling and mining efficiencies. Plenty of studies have focused on the erosion behavior features of the cavitating jet. Two peaks of the specimen mass loss with the increasing standoff distance have been observed by Liu et al. (2020), Yamaguchi and Shimizu (1987), Momma and Lichtarowicz (1995). The erosion pattern of the first peak exhibits two isolated ringlike

erosion regions, which gradually merge into one single erosion ring at the second peak (Yamauchi et al., 1995; Liu and Ma, 2021). A lot of rock-breaking theories including cavitation fragmentation (Crow, 1973), crack extension crushing (Forman and Secor, 1974) and tensile-wedge effect (Li and Shen, 2005) have been validated, whereas the rock-breaking mechanism is still far from being understood due to the rock inhomogeneity. Recently, Jasper et al. (2021) experimentally studied the cavitating jet drilling process in the ambient condition with erosion damage test and flow visualization. They suggested that the cavitation cloud impingement primarily contributes the erosion damage rather than the water hammer effect. Experiments on sandstone by Chen et al. (2023) indicated that the increasing erosion period extends the action time of the cavitating jet in the main erosion area, resulting in severer damage. Fan et al. (2023) reported that the irregular shape of the erosion region is generated by the cavitation bubbles collapse. Cai et al. (2023) observed similar funnel-like erosion regions of basalt, granite and sandstone under the cavitating jet impingement.

The flowing motion features of the cavitation cloud directly decide the erosion result of the jet. The cavitation cloud formation

* Corresponding author.

E-mail address: liuboshen@ustb.edu.cn (B.-S. Liu).

occurs in the shear layer and which further develops to a ring shape throughout the impingement under the effects from stagnation area and wall jet (Yamaguchi and Shimizu, 1987; Liu and Ma, 2021; Soyama, 2017). The flow visualization experiment was conducted by Sato et al. (2009) for the impingement process of the cavitation cloud, where two kinds of clouds were observed including the main impinging cloud and the outward spreading scattered cloud. Soyama et al. (2011) and Kang et al. (2018) used the polyvinylidene fluoride (PVDF) to achieve the impact pulse of the bubble collapse. They indicated that the aggressive ability is proportional to the cavitation impact energy. Peng et al. (2018) classified the cavitation cloud motion features with proper orthogonal decomposition (POD) and suggested that the intensities of concentrated bubbles and collapse events decide the cavitation intensity. Liu and Ma (2021) explored the erosion mechanism under the inclined jet impingement, where partial severe erosion damage was generated by the restricted spreading cavitation clouds. Attention was also placed on the cavitation erosion mechanism in the microscopic view. Early study by Tomita and Shima (1986) demonstrated that the erosion pit induced by the single bubble collapse is essentially generated by the impact pressure from a liquid microjet. Chahine and Hsiao (2015) indicated that the impulsive impact on the material is damped with the material surface deformation. Chi et al. (2022) suggested that for the sedimentary rock, such as shale, the microstructure of rock under the impact from single bubble collapse experiences a brittle failure process without plastic deformation. Recently, Wu et al. (2023a) numerically investigated the single cavitation bubble collapse behaviors near a hydrate surface, where they found the shock wave has a greater contribution than the micro-jet in the erosion process. Due to the fragility of the rock, the erosion valley generated in a very short period is deep enough to significantly affect the impinging flow. Despite lots of precious studies have focused on revealing the cavitation jet breaking mechanism on rock, the cavitation clouds impingement features and the cloud motion characteristics under the influence from varying eroded rock surface have not been thoroughly explored.

In this work, in order to realize the full potential of the cavitating jet at rock breaking in the underground petroleum exploitation, we explored the aggressive ability of the jet with serial erosion tests and flow visualization across a wide range of standoff distance ratios. In particular, the cavitation cloud impingement motion in the each erosion development stages was experimentally investigated with flow visualization. We employed a X-ray computerized tomography (CT) and a high-speed camera to reveal the erosion damage, cavitation cloud motion and their interactions during the rock breaking process. The experimental setup of erosion measurement and flow visualization is specified in Section 2, the results are presented and discussed in Section 3, whereas the conclusions are given in Section 4.

2. Experimental setup

2.1. Cavitating jet apparatus

The erosion test and flow visualization system are presented in Fig. 1(a). The test section of the vessel was 22 cm in each dimension. The upstream feeding pressure generated by a plunger pump was $p_i = 12.6$ MPa. The ambient pressure controlled by the downstream relief valve was set at $p_e = 0.6$ MPa. The cavitation number $\sigma_n = (p_e - p_v)/(p_i - p_e)$ was adjusted to 0.05 for the serial tests, where p_v is the vapor pressure of the water. Three pressure transducers were installed in the injection pipe, the testing vessel and the ejection pipe with uncertainties of 0.25%. The water temperature was 28 ± 1 °C. The serial tests were performed at various exposure

periods $T_e \in [15 \text{ s}, 135 \text{ s}]$. The cavitating jet was produced by the organ-pipe nozzle presented in Fig. 1(b) (Liu et al., 2020, 2022; Liu and Ma, 2021). The specific parameters of the nozzle configuration are listed in Table 1. The specimen Cartesian coordinate system consists of the symmetrical axis z and the surface outward radial direction x . The standoff distance l_s was defined as the length from the nozzle bottom to the surface of the specimen. The dimensionless standoff distance ratio $l_d = l_s/d_n$ was adopted in this research in the range of $l_d \in [2, 16]$.

2.2. Erosion measurements

The mechanical properties of the artificial sandstone specimen are listed in Table 2, which has been widely adopted in related research (Fan et al., 2023; Kang et al., 2023). According to the test results, the erosion damage on sandstone was generated in a very short exposure period T_e and the specimen topographical variation significantly influenced the cavitation flow characteristics in the jet impingement process. To reveal the cavitation cloud motion characteristics during the initial jet impingement, the additional flat specimen made of stainless steel was adopted to exclude the influence from the dramatic topographical variation of eroded sandstone on the flow. The diameter of the specimen disc was $d_s = 40$ mm. The exposure periods of the sandstone and the stainless steel under the cavitation impingement at each standoff distance ratio were $T_e = 90$ s and 30 s, respectively. In addition, the erosion development on the sandstone was individually investigated at the increasing $T_e \in [0, 135 \text{ s}]$.

The mass loss generated by the cavitation erosion damage and the eroded surface topography were employed as the representative features of the jet's aggressive ability (Liu et al., 2020; Yamaguchi and Shimizu, 1987). Each test was conducted four times to ensure the reliability of the results. The mass loss Δm of the specimens was measured after air-drying. The erosion boundary of the sandstone specimen was obtained by the grayscale threshold calculation according to the specimen photo, which was scanned by an HP ScanJet printer. The spatial geometry of the erosion region in sandstone specimens was obtained by an X-ray computerized tomography (CT), Sanying nanoVoxel-3000 (Liu and Ma, 2021). The CT slices were achieved at the spatial resolution of 31.07 μm , which were further combined to rebuild the 3D erosion region with $1600 \times 1600 \times 1440$ pixels.

2.3. Flow visualization

A high-speed camera Phantom VEO 410L with a sampling frequency of 20000 FPS was used to capture the cavitation cloud flowing motion (Wu et al., 2022). The cavitation clouds were illuminated by a high-lumen LED lamp located on the opposite side of the camera. The camera and the lamp were located at $l_c = 200$ mm and $l_l = 140$ mm away from the nozzle axis, respectively (Fig. 1(a)). The flow visualization photographs were processed with the format in uint-8, where the photo scale was 256×512 pixels and the limitation of grey-scale was $[0, 255]$. To ensure the adequate sample capacity, the exposure period of the flow visualization measurement was 1 s.

To investigate the instantaneous flowing features of the cavitation clouds in the erosion crater, the trinity eroded specimen was reconstructed by 3D printing based on the rebuilt erosion region model, as shown in Fig. 2. It was assumed that the target surface being eroded of sandstone during the flow visualization testing period have little influence on the cloud motion features. The top of the reconstructed specimen was made of transparent photocurable resin for flow visualization and the middle was printed by stainless steel to resist the cavitation cloud impingement. The bottom was

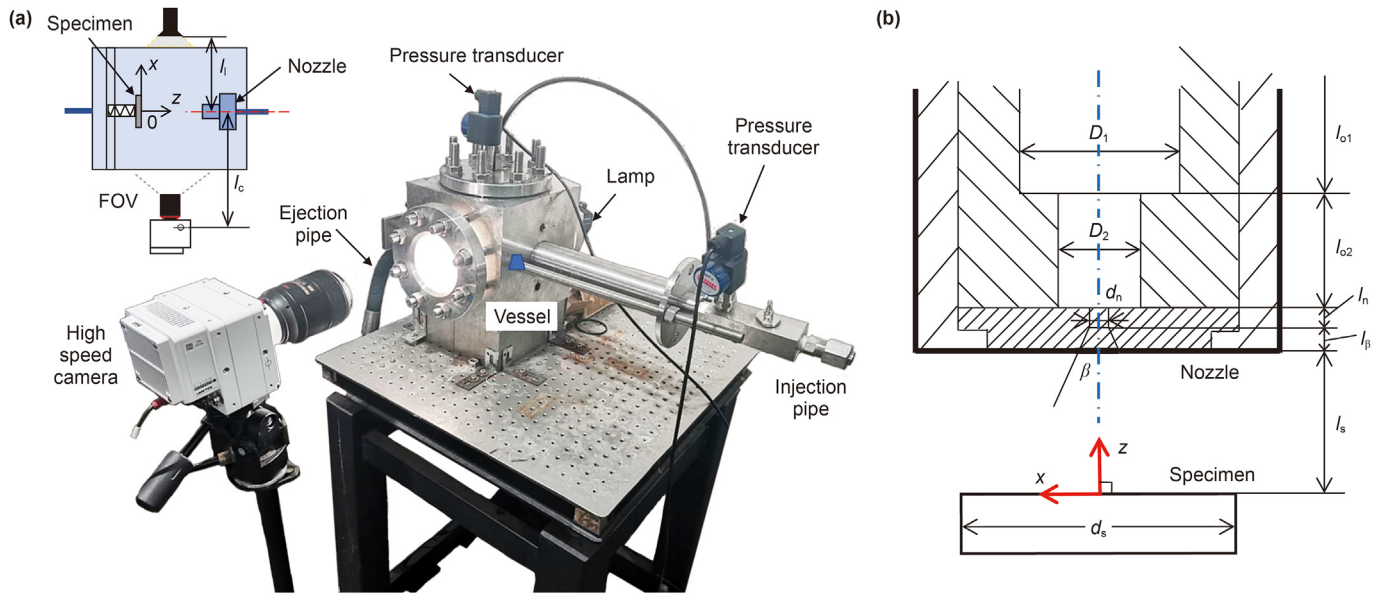


Fig. 1. (a) Erosion test and flow visualization system and (b) nozzle geometry.

Table 1
Nozzle dimensions.

Dimensions, mm	D_1	D_2	d_n	l_{o1}	l_{o2}	l_n	l_β	$\beta, ^\circ$
Value	24	10	2	70	42	0.7	2.8	20

printed by high-strength nylon to support the combined specimen. The cavitation clouds need to be separated from the transparent photocurable resin samples to observe the morphology of cavitation clouds more clearly using the image processing method, as illustrated in Fig. 3. First, the background was subtracted from the original image to get the outline of the cavitation clouds. To facilitate the following watershed processing algorithm, the image pixel inversion operation was carried out. The resulting images need to be preprocessed to benefit image segmentation, in which gamma transform was used to enhance the image and Gaussian transform (Gaussian filtering) was used to remove noise. Finally, the watershed algorithm was used to segment the whole cavitation cloud edge.

3. Results and discussion

3.1. Mass loss and erosion pattern

To inspect the erosion features of the cavitating jet on the sandstone, the averaged mass loss Δm_s with increasing l_d is shown in Fig. 4. Two peaks of Δm_s were observed at the two optimum standoff distance ratios $l_d = l_1 = 5$ and $l_d = l_2 = 10$, where the jet erosion ability is stronger than other l_d (Soyama, 2017). Further, the second peak of Δm_s at downstream l_2 induced by a severer erosion damage is higher than the first peak obtained near the nozzle exit l_1 . Similar double peaks of specimen mass loss were reported by Chi et al. (2022) and Ge et al. (2011) in rock breaking, where the

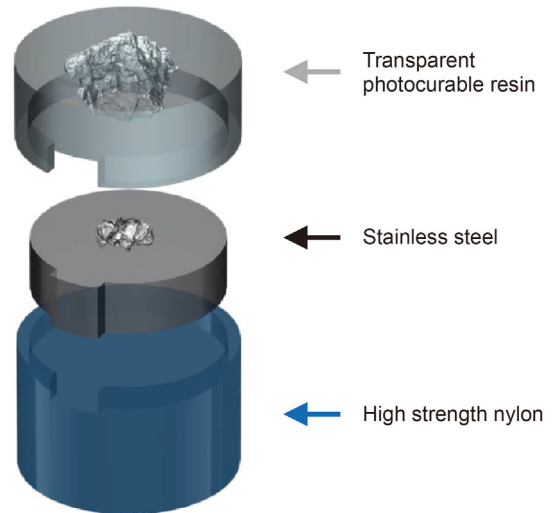


Fig. 2. Erosion region reconstruction by 3D printing.

cavitation numbers were set in $\sigma_n \in [0.0025, 0.06]$.

The erosion damage generated by the cavitating jet on the sandstone specimens is shown in Fig. 5 and the erosion topography at selected standoff distance ratios is shown in Fig. 6. At $l_d = 2$, one shallow crater was generated on the sandstone, as presented in Fig. 5(a), labeled as ES. In Fig. 5(b), a deeper erosion crater ES in a U-shaped cross section (Fig. 6(a)) is observed at $l_1 = 5$, corresponding to the first peak of mass loss Δm_s induced by the enhanced aggressive ability of the jet. The jet's aggressive ability slightly decreases at $l_d = 6$ and the ES was observed as a larger shallow U-shaped erosion crater. The bottom cleaning effect is observed in the

Table 2
Mechanical and physical properties of the artificial sandstone specimen.

Material	Erosion strength, MPa	Compression strength, MPa	Elastic modulus, GPa	Poisson's ratio	Rock-cohesion, MPa
Sandstone	3.49–4.42	65.03–65.68	137.77–138.66	0.19	15.86

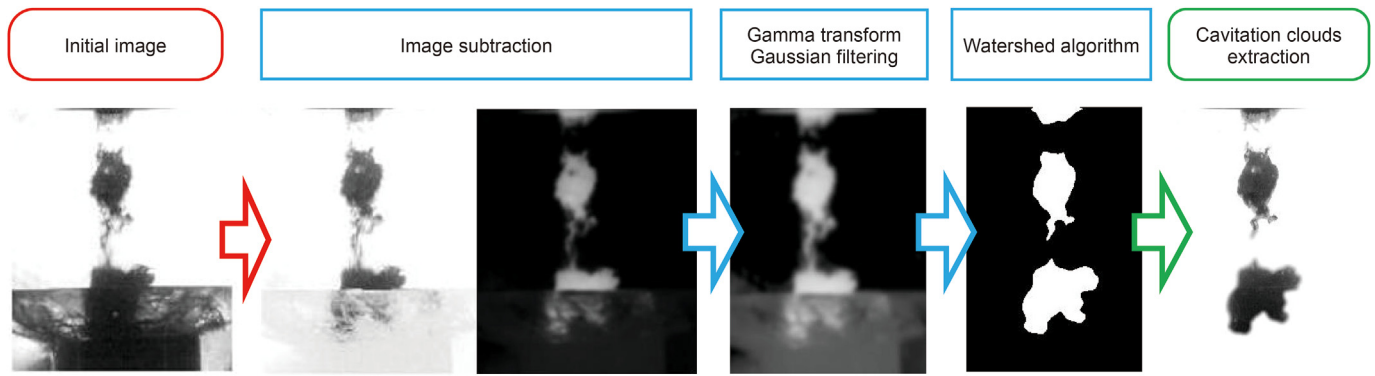


Fig. 3. Diagram of image processing.

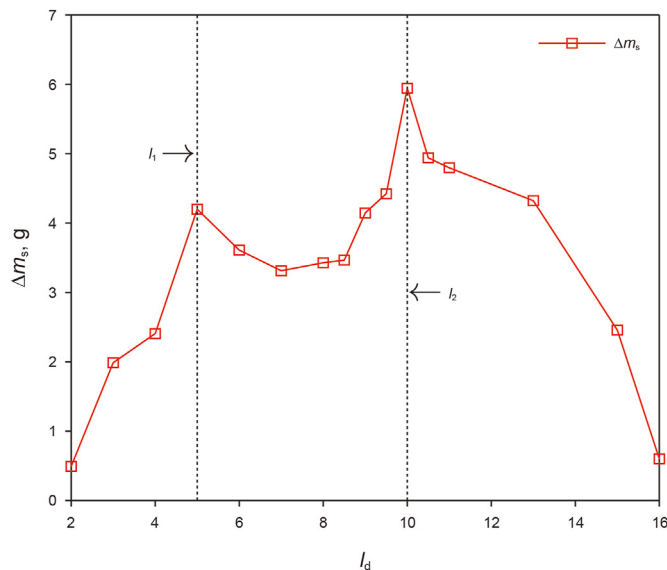


Fig. 4. Mass loss of the sandstone Δm_s at a series of standoff distance ratio $l_d \in [2, 16]$.

range of pattern A, the eroded surface of the damage crater is smoother than the other standoff distance ratios (Wu et al., 2023b). With the increase of l_d , the erosion damage returns to the deep valley shape at $l_d = 9$. The severest erosion was achieved at $l_2 = 10$, where the jet achieved the strongest aggressive ability, as presented in Figs. 5(f) and Fig. 6(c). The jet aggressive ability dramatically shrunk with longer standoff distances, which resulted in a larger and shallower ES on the sandstone, as presented in Figs. 5(h) and Fig. 6(d) at $l_d = 16$.

To get insight into the jet erosion features on the sandstone, the equivalent erosion radius on sandstone R_{es} and the maximum erosion depth h_{emax} are summarized in Fig. 7. The equivalent radius R_{es} is calculated by $R_{es} = (A_e/\pi)^{0.5}$, where A_e is the projected area of erosion damage on the $x - y$ plane. The erosion damage was divided into three patterns according to R_{es} , h_{emax} and Δm_s . In pattern A, $l_d \in [2, 5]$, the equivalent radius R_{es} decreases with higher h_{emax} . At the beginning of pattern B, $l_d = 6$, R_{es} extends with the dramatic decrease of h_{emax} , indicating that the erosion ability is slightly suppressed at $l_d = 6$. With increasing $l_d \in [6, 10]$, h_{emax} rebounds significantly and reaches the maximum at $l_2 = 10$, but the erosion radius R_{es} increases in low amplitudes. In pattern C, $l_d \in [11, 16]$, the increasing standoff distance diminishes the aggressive ability of the cavitating jet, which results in the border and

shallower erosion area with a larger R_{es} .

3.2. Cumulative erosion features

Fig. 8 shows the cumulative erosion rate (CER) $\epsilon = \Delta m_s/T_e$ of the erosion on sandstone at the optimum standoff distance ratio $l_2 = 10$. The serial testing exposure periods were controlled at $T_e \in [15 \text{ s}, 135 \text{ s}]$ with an interval $\Delta T_e = 5 \text{ s}$. The cumulative erosion rate of sandstone generated by the cavitating jet can be divided into three stages, acceleration stage $T_e \in [15 \text{ s}, 35 \text{ s}]$, deceleration stage $T_e \in [35 \text{ s}, 65 \text{ s}]$ and terminal stage $T_e \in [65 \text{ s}, 135 \text{ s}]$ (Choi et al., 2012).

In the acceleration stage, the cavitation clouds directly impinges on the sandstone quasi flat surface and induce erosion damage immediately. With the developing erosion damage, as show in Fig. 9(a) at $T_e = 30 \text{ s}$, the acceleration stage ended once the surface of eroded region already had a significant variation, where the varying surface of the erosion crater affects the cavitation cloud motion (Liu and Ma, 2021). The entrapped two-phase flow on the erosion valley bottom starts to cushion the impingement and suppress the bubble collapse, which results in the deceleration stage. Finally, the erosion process get into the terminal stage. At the longer erosion exposure period T_e shown in Fig. 9(c) at $T_e = 135 \text{ s}$, the maximum erosion depth has reached $h_{emax} = 19.58 \text{ mm}$ where the bulk of bubbles have already collapsed before impinging on the target, resulting in the lower CER ϵ . As shown in the cross-section in Fig. 9(c), the reaming effect is observed, where the erosion crater shrinks first then extends in the radial direction and finally undergo a rapid reduction (Wu et al., 2023a).

3.3. Cavitation cloud motion feature

The strength of the cloud formation and collapse is evaluated by the standard deviation of the cavitation clouds volume fraction σ , which is calculated according to the grey-scale statistics of the flow photographs (Liu and Ma, 2021; Gavaises, 2008; Mitroglou et al., 2014). The cavitation cloud motion is illustrated by a series of instantaneous photographs of the cavitating jet, where T_e' is the relative exposure period and the interval period Δt_e is $43.47 \mu\text{s}$. Parts of the x -axis ticks are highlighted for better identification. The scope of erosion on sandstone ES is presented according to the equivalent erosion radius R_{es} .

Fig. 10(a) presents the standard distribution of σ at $l_d = 2$ (pattern A) in the initial jet impingement process, where the concentrated σ is observed approximately match the erosion region ES. The dynamic motion of the cavitation cloud is illustrated in Fig. 10(b)–(i). First, as shown in Fig. 10(b), the cavitation cloud (CC)

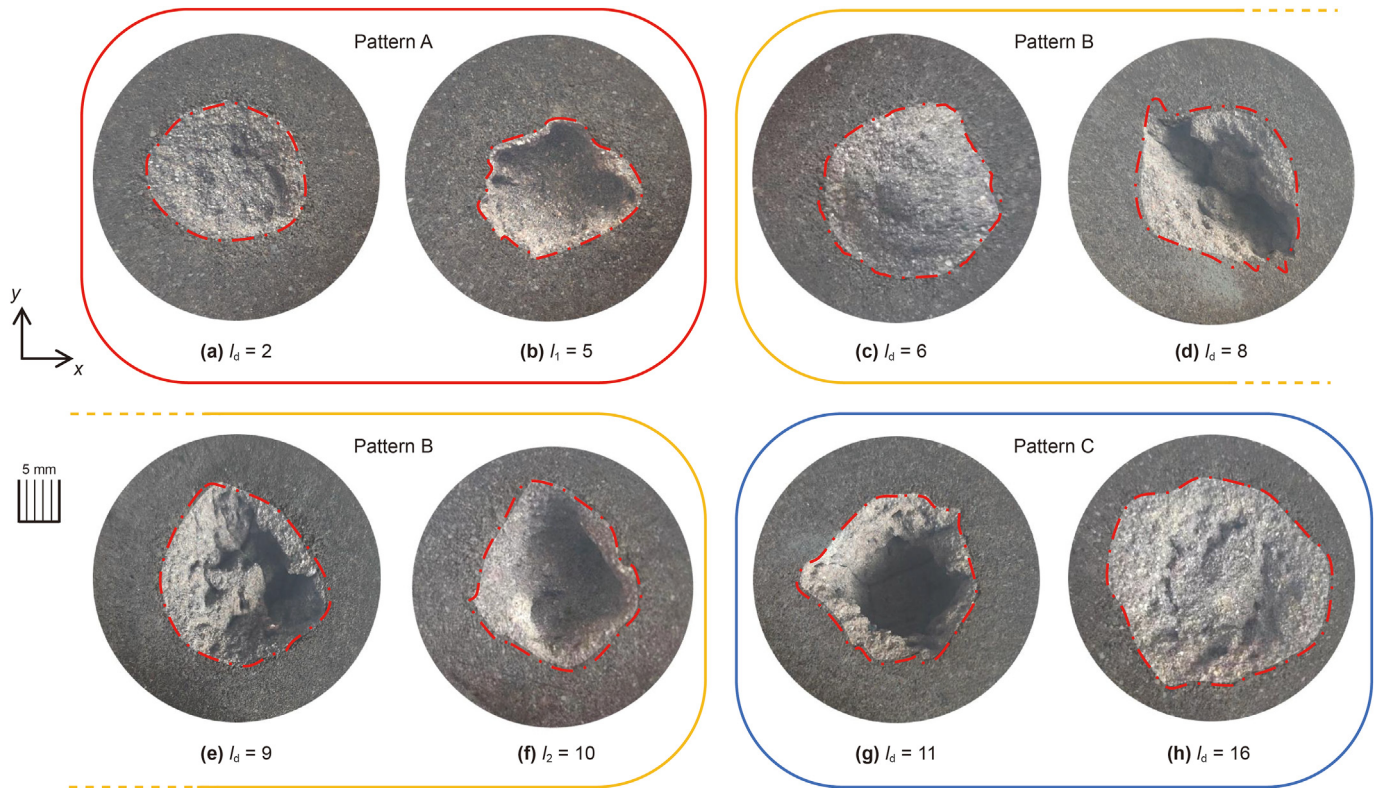


Fig. 5. Photographs of the erosion damage induced by the cavitating jet on sandstone. (a) $l_d = 2$, (b) $l_1 = 5$, (c) $l_d = 6$, (d) $l_d = 8$, (e) $l_d = 9$, (f) $l_2 = 10$, (g) $l_d = 11$, (h) $l_d = 16$.

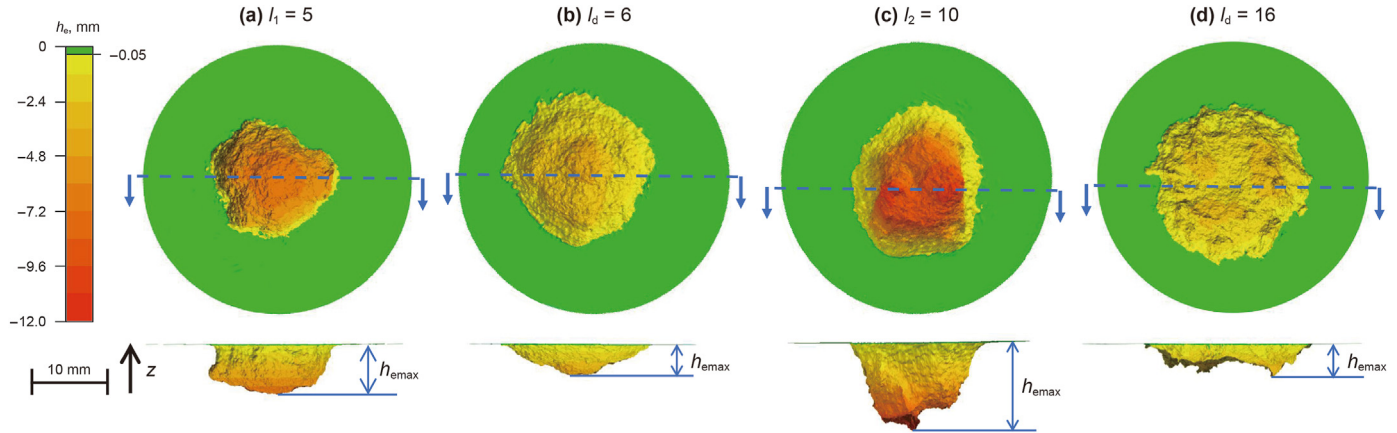


Fig. 6. Normal view and cross section of the sandstone erosion topography, $T_e = 90$ s. (a) $l_1 = 5$, (b) $l_d = 6$, (c) $l_2 = 10$, (d) $l_d = 16$.

shedding from the nozzle impinges on the target surface due to the short standoff distance. In Fig. 10(c)–(i), some scattering clouds are washed away by the wall-jet, which spread outwards along the target flat surface and collapse at further radial locations. Similar cavitation cloud motion was observed by Sato et al. (2009) and Soyama et al. (1995).

As presented in Fig. 11, the geometrical alteration of impinging target surface in ES was reconstructed by stainless steel with 3D-printing according to the CT scanning result of the eroded sandstone. The distribution of σ of the eroded sandstone at $l_d = 2$, $T_e = 90$ s is shown in Fig. 11(a), where the concentrated σ spreads slightly upwards and disperses right outside the boundary of erosion crater. Fig. 11(b)–(i) present the corresponding serial instantaneous photographs during the impingement. As shown in

Fig. 11(d)–(f), the erosion crater was deep enough to redirect the wall-jet after cloud impingement, where the scattering cavitation clouds spread along the erosion crater surface. This phenomenon indicates that at the low standoff distance ratio $l_d = 2$, the erosion damage on the sandstone is generated by the bubbles collapse in two subdivided processes, the impingement and the scattering. In the initial period of erosion, the damage is generated by the cavitation clouds impingement. Further, due to fragility of sandstone, the erosion crater is generated rapidly and the concave ES restricts the outward spreading of the scattering CC. Finally, the scattering clouds collapse during the spreading process which extends the ES, which in turn dramatically changes the features of the cavitation cloud motion. The strong outward scattering of the cavitation clouds resulting in the erosion crater of a higher R_{eS} but a lower

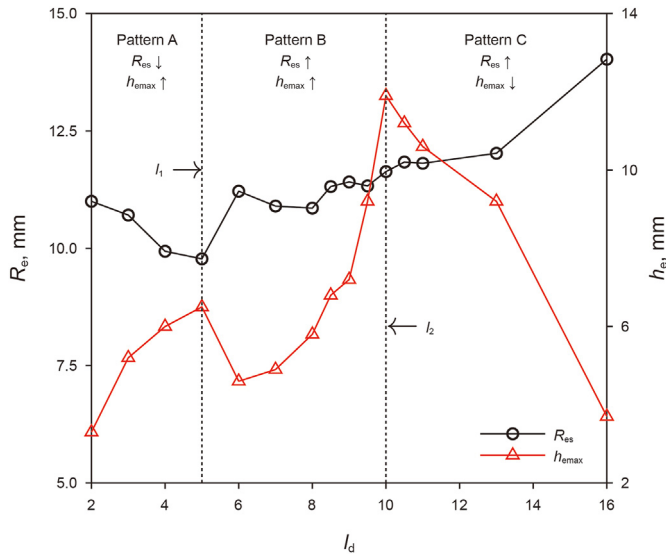


Fig. 7. The equivalent outline radius R_{es} and the maximum erosion depth h_{emax} .

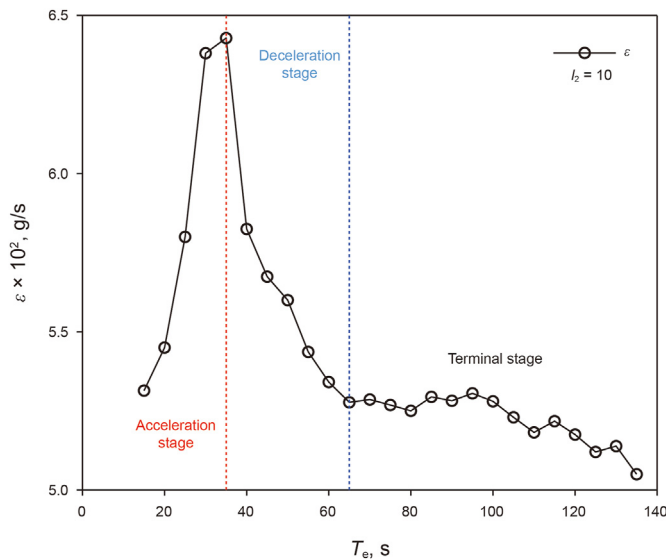


Fig. 8. Cumulative erosion rate ϵ of the erosion on sandstone at $l_2 = 10$, $T_e \in [15, 135]$ s].

h_{emax} , namely the wide and shallow rock breaking features in damage pattern A (Fig. 5). Furthermore, the strong scattering CC scours the eroded surface, causing the bottom cleaning effect (Wu et al., 2023b). The rest of the scattering clouds vanish above the surface without generating any erosion damage.

Fig. 12 presents the standard deviation of the cavitation clouds σ and the selected instantaneous photographs in the initial jet impingement process at $l_d = 5, 6, 8, 10, 16$, respectively. As presented in Fig. 12(a1) at the first optimum standoff distance ratio $l_1 = 5$, the cavitation clouds achieve a better advancement and which induces the first peak of mass loss as shown in Fig. 4. It is noted that in pattern A, the high σ region ($\sigma > 100$) is clearly separated by the inner high-speed water column, which develops in a concentric ring-like manner (Liu et al., 2020; Soyama et al., 1995).

In erosion pattern B at $l_d = 6$, as shown in Fig. 12(b1), the high σ region starts to merge together before impingement, where the

cavitation strength is enhanced comparing to which in pattern A. Furthermore, σ of the radially scattering clouds is advanced in the initial impingement, which enlarges the erosion and induces the higher equivalent radius R_{es} . At $l_d = 8$, the high σ region merges together before impinging on the target, as shown in Fig. 12(c1), where the wall jet at $l_d = 8$ is still strong enough to generate the scattering clouds (Fig. 12(c2)). At the second optimum standoff distance $l_2 = 10$, as depicted in Fig. 12(d1), the cavitation clouds have an essential development before impingement. Due to the decelerated wall jet induced by the larger l_d , the cavitation clouds are more concentrated and which vanishes after the impingement without generating the scattering clouds (Fig. 12(d2)). The cavitation clouds concentration before impingement generates the erosion crater of a higher maximum erosion depth h_{emax} , while the scattering motion is diminished resulting in the increasing R_{es} in low amplitudes in damage pattern B (Fig. 7).

Fig. 12(e1)–(e2) shows the distribution of σ and the instantaneous photographs at $l_d = 16$ in pattern C, which is close to the effective standoff distance of the jet. The cavitation clouds are fully developed and most of which collapses before impinges on the target surface, causing the decreasing h_{emax} in damage pattern C. At $l_d = 16$, the aggressive ability of the jet is in a low level and which does not generate the deep erosion crater. The residual cavitation clouds collapse during the spanwise spattering induces the sustained increase of R_{es} , which results in the larger but shallower erosion crater in damage pattern C.

The standard deviation of cloud fraction just before impingement σ_c and the corresponding dominating frequency of the fluctuating fraction f_d are summarized in Fig. 13(a), providing the influence of the standoff distance on the cavitating jet flow. The grey-scale pulse was obtained at $\Delta l_d = 0.4$ above the target surface along the z axis, $x/d_n = 1.5$. In the range of $l_d \in [2, 10]$, pattern A and B, the increasing standoff distance induces a higher fluctuation of the cloud volume fraction σ_c , suggesting that the larger nozzle-target space results in the better cavitation cloud development. At $l_d = 16$, a lower σ_c is obtained due to the overlong l_d . The observed distinctive reduction of the dominant frequency f_d indicates that the impingement frequency is attenuated with the increasing l_d . Furthermore, the impingement strength of the cavitation cloud is obtained by $\sigma_f = \sigma_c \times f_d$, where two peaks of σ_f are detected at the two corresponding optimum standoff distance ratios $l_1 = 5$ and $l_2 = 10$ as depicted in Fig. 13(b). It provides an explanation for the existence of the dual peak mass loss that the cavitation strength is low at $l_1 = 5$ but the impingement frequency is high enough to generate the severe erosion. Moreover, at $l_2 = 10$, the better developed cavitation clouds enhance the erosion ability of the jet even at a lower impingement frequency.

The modulation of developing eroded surface has a dramatic effect on the cavitation cloud motion. The cavitation cloud motion features in the developing sandstone erosion crater of the second optimum standoff distance ratio $l_2 = 10$ was investigated at selected exposure period $T_e = 30, 90$ and 135 s, as show in Figs. 14–16, respectively. At $T_e = 30$ s, as presented in Fig. 14(d), a lump of scattering cavitation cloud was observed during the impingement. The scattering clouds accompanied with the redirected wall jet spread upwards induced by the curve sidewall of the erosion crater. However, most of the scattering clouds are restricted and collapse in the crater due to the high erosion depth, suggesting that the erosion is induced by the bubbles collapse in both of the impinging and restricted scattering processes at the acceleration stage of CER ϵ (shown in Fig. 8). With the exposure period increasing to $T_e = 90$ s in the terminal stage, the larger erosion depth reduces the velocity of the wall jet and enhances the cushion effect at the crater bottom, which induce the shrinking region of high σ (shown in Fig. 15(a)). In Fig. 15(e)–(g), the restricted scattering cavitation clouds still could

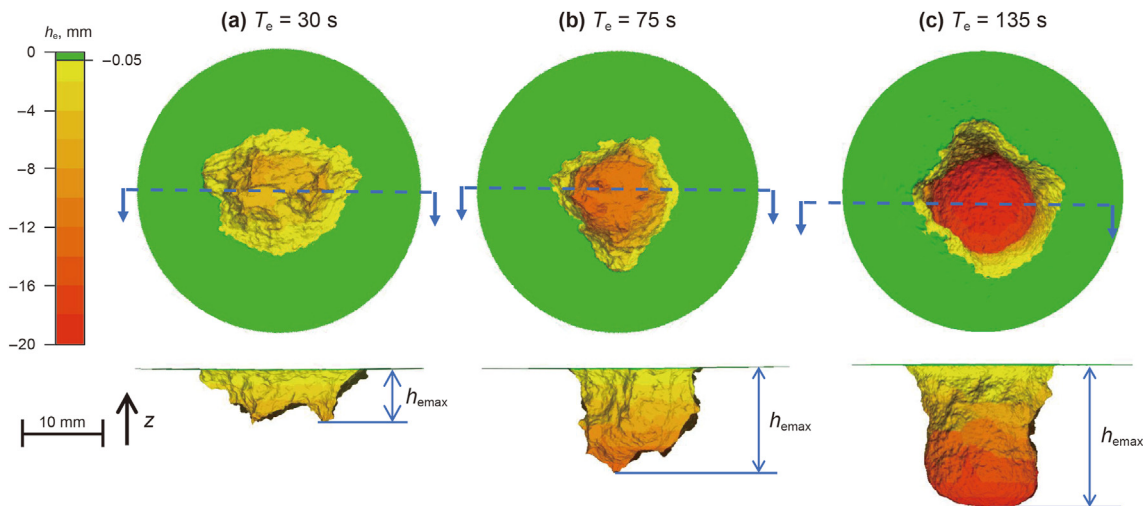


Fig. 9. Erosion development on the sandstone at $l_2 = 10$ with increasing exposure period, (a) $T_e = 30$ s, (b) $T_e = 75$ s, (c) $T_e = 135$ s.

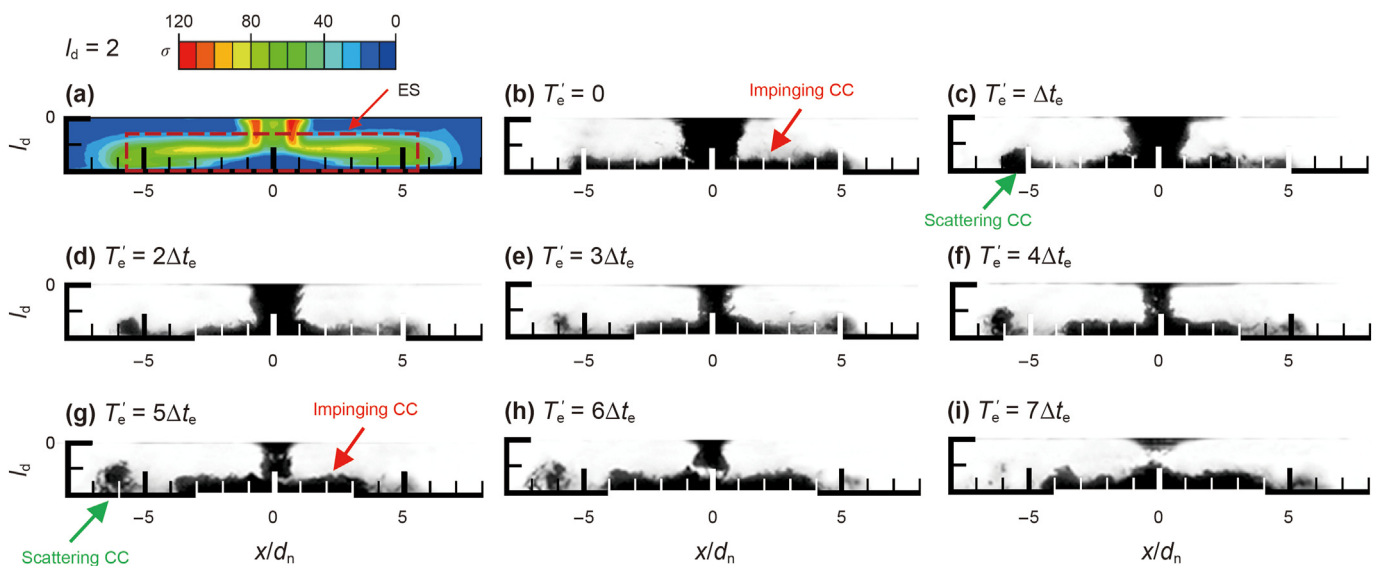


Fig. 10. (a) Standard deviation of the cavitation clouds σ at $l_d = 2$ (pattern A) in the initial jet impingement process. (b)–(i) Instantaneous photographs in the process of the cavitation cloud impingement.

be observed with lower strength. At $T_e = 135$ s, as shown in Fig. 16, the erosion was primarily induced by the impinging cavitation clouds, where the bulk of bubbles have already collapsed before impinging on the target, which results in the lower CER and the reaming effect.

4. Conclusions

The cavitation cloud impingement and scattering motion of the cavitating jet in the sandstone erosion process was experimentally explored with serial erosion test and flow visualization measurement. Two mass loss peaks generated by the erosion damage on sandstone are observed at the corresponding optimum standoff distance ratios. Various erosion patterns are identified based on the eroded specimen topography. In the lower range of standoff distance ratio $l_d \in [2, 5]$ in pattern A, the combination of impinging and scattering cavitation clouds generate the shallow erosion crater. The increase of l_d promotes the development of cavitation

cloud but reduces the frequency of impingement. The jet aggressive ability is enhanced when the balance between the cavitation cloud development and the impingement frequency is reached. The severest damage is observed at $l_2 = 10$, where the erosion is induced by the concentrated and developed cavitation clouds impingement. The whole erosion process presents as three stages, acceleration, deceleration and terminal steady stage according to the cumulative erosion rate. The instantaneous features of cavitation cloud motion in the erosion crater of different stages were investigated with the transparent specimen designed according to the reconstructed results of CT scanning. The erosion in the crater at shorter exposure periods T_e is generated by the combination of impingement and restricted scattering of cavitation clouds due to the high gradient eroded sidewall. The jet aggressive ability is diminished by the erosion depth expansion on sandstone at a longer T_e , where the cavitation clouds impinge on the target and then collapses and vanishes without restricted scattering. The cloud impingement and scattering motions directly influence the

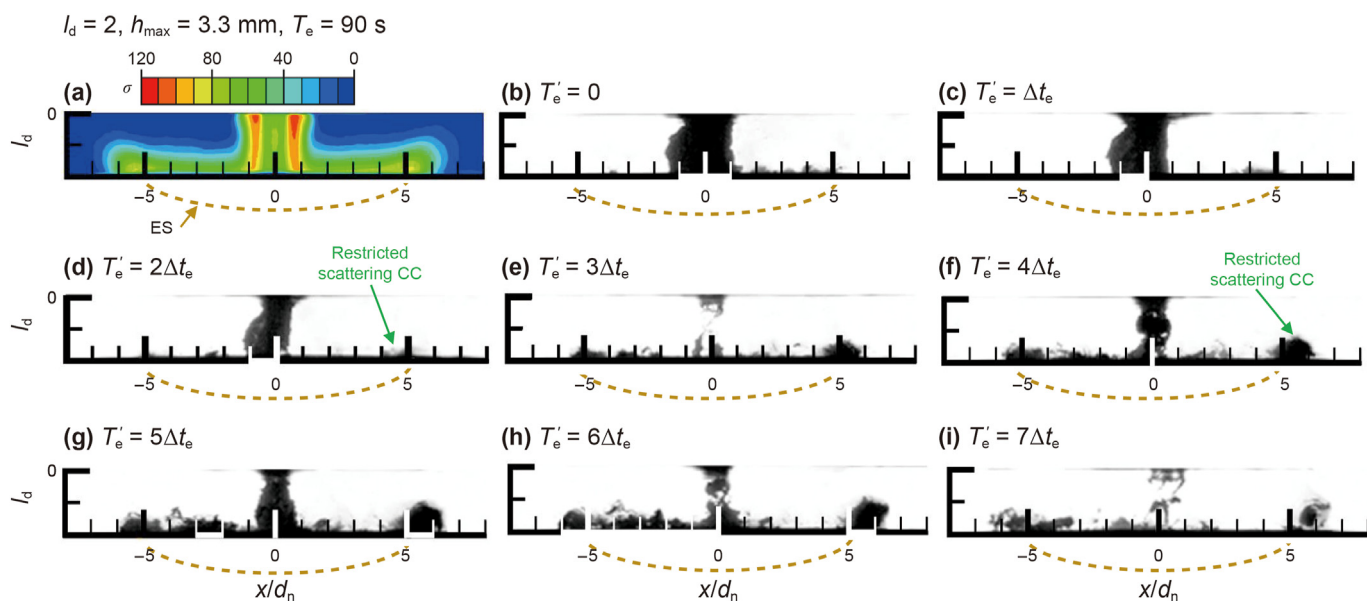


Fig. 11. (a) Standard deviation of the cavitation clouds σ at $l_d = 2$ (pattern A) for the eroded sandstone, $T_e = 90$ s. (b)–(i) Instantaneous photographs in the process of the cavitation cloud impingement. The reconstructed erosion region ES is highlighted with dash line.

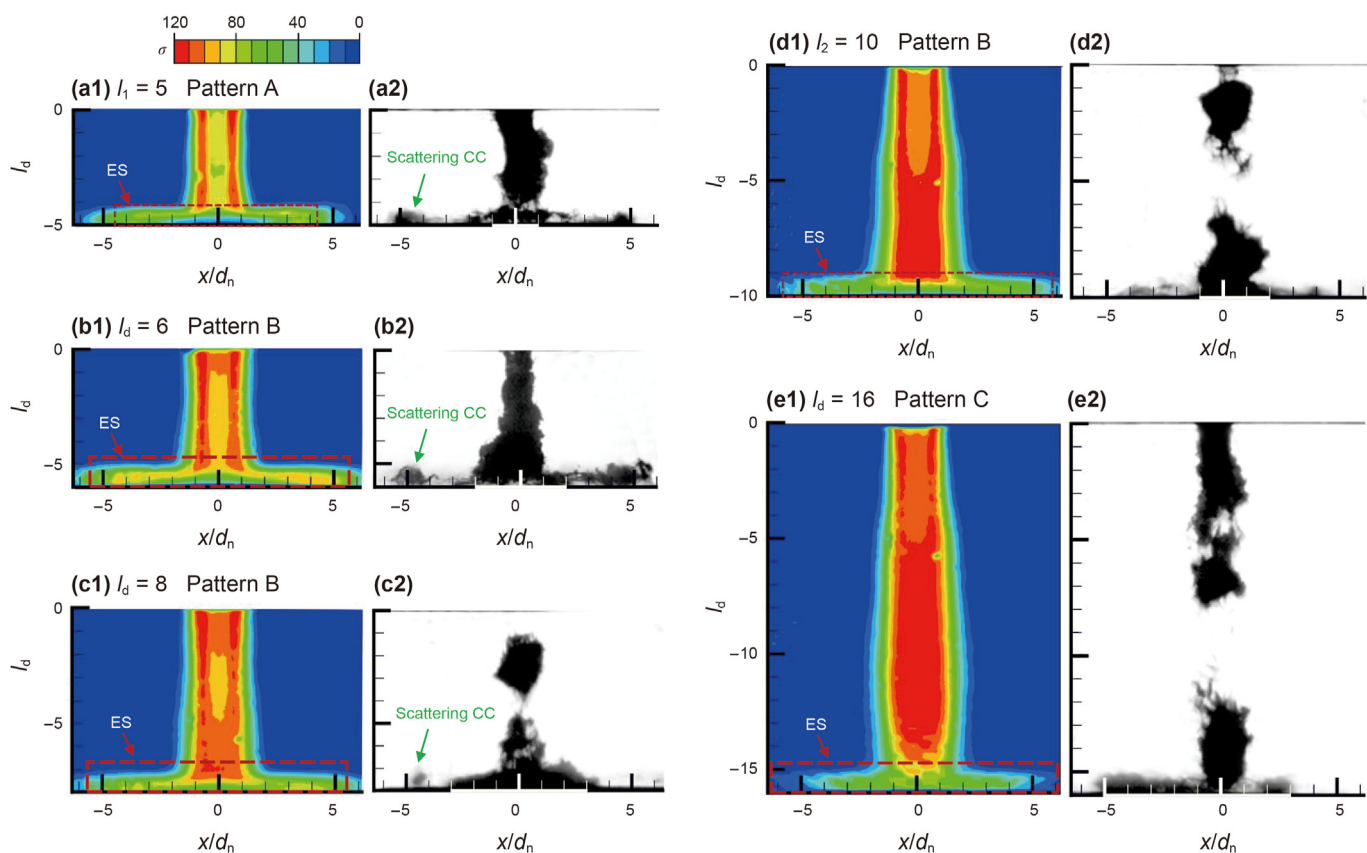


Fig. 12. (a1) Standard deviation of the cavitation clouds σ at $l_1 = 5$ (pattern A) in the initial jet impingement process, (a2) selected instantaneous photographs at $l_1 = 5$. (b1)–(b2) σ and instantaneous photographs at $l_d = 6$, pattern B. (c1)–(c2) σ and instantaneous photographs at $l_d = 8$, pattern B. (d1)–(d2) σ and instantaneous photographs at $l_2 = 10$, pattern B. (e1)–(e2) σ and instantaneous photographs at $l_d = 16$, pattern C.

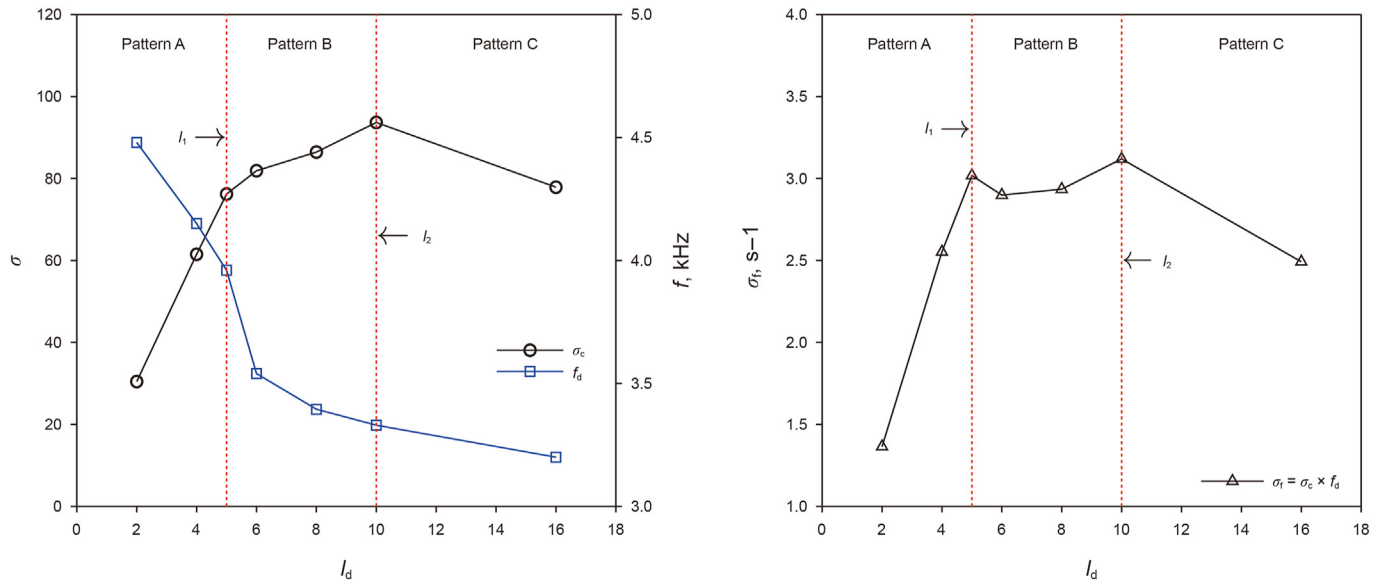


Fig. 13. (a) Standard deviation of the cavitation clouds and the corresponding dominating frequency before impingement. (b) Impingement strength.

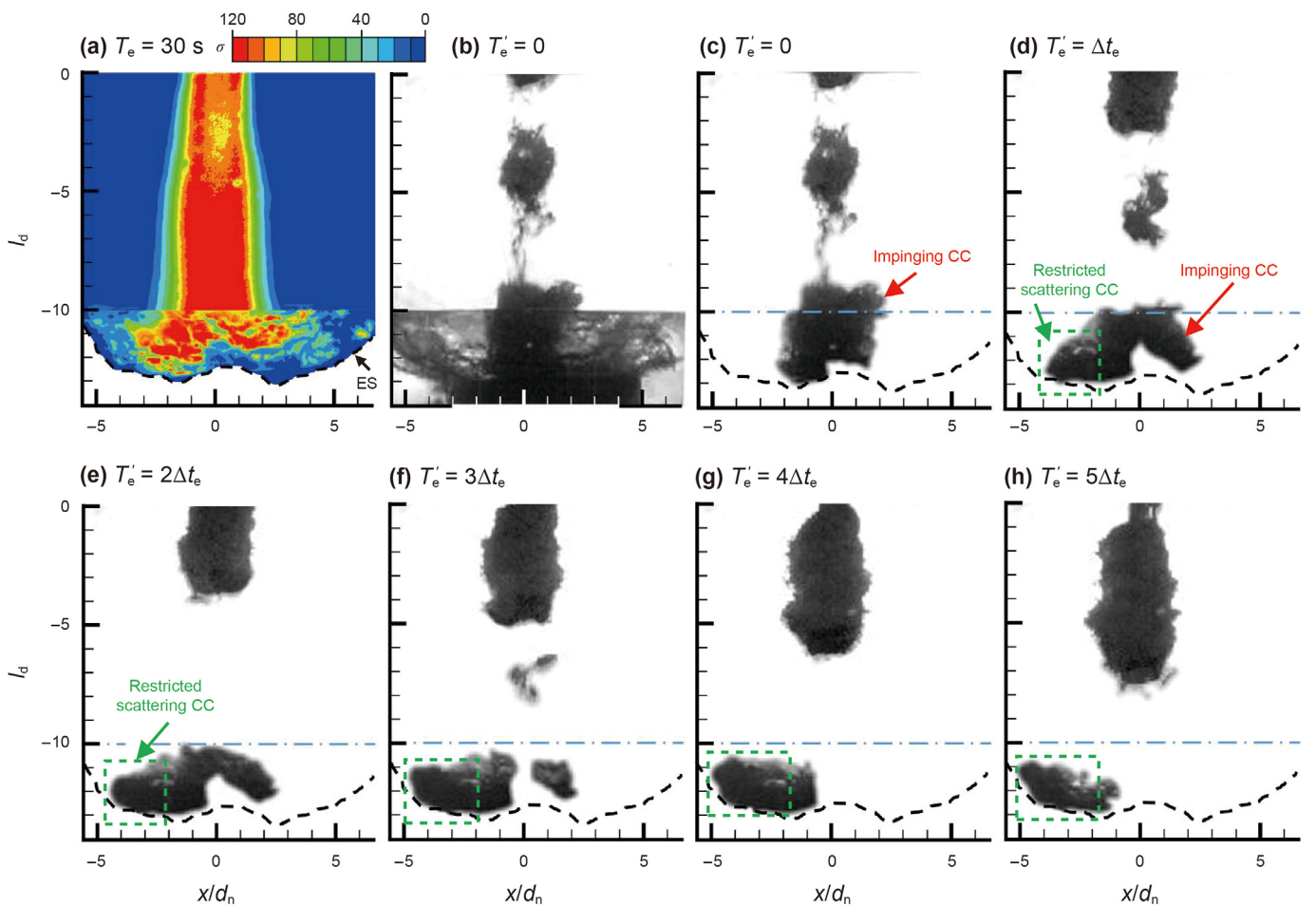


Fig. 14. (a) Standard deviation of the cavitation clouds at $l_1 = 10$ for the erosion at $T_e = 30$ s. (b) Original instantaneous photographs. (c)–(i) Instantaneous photographs.

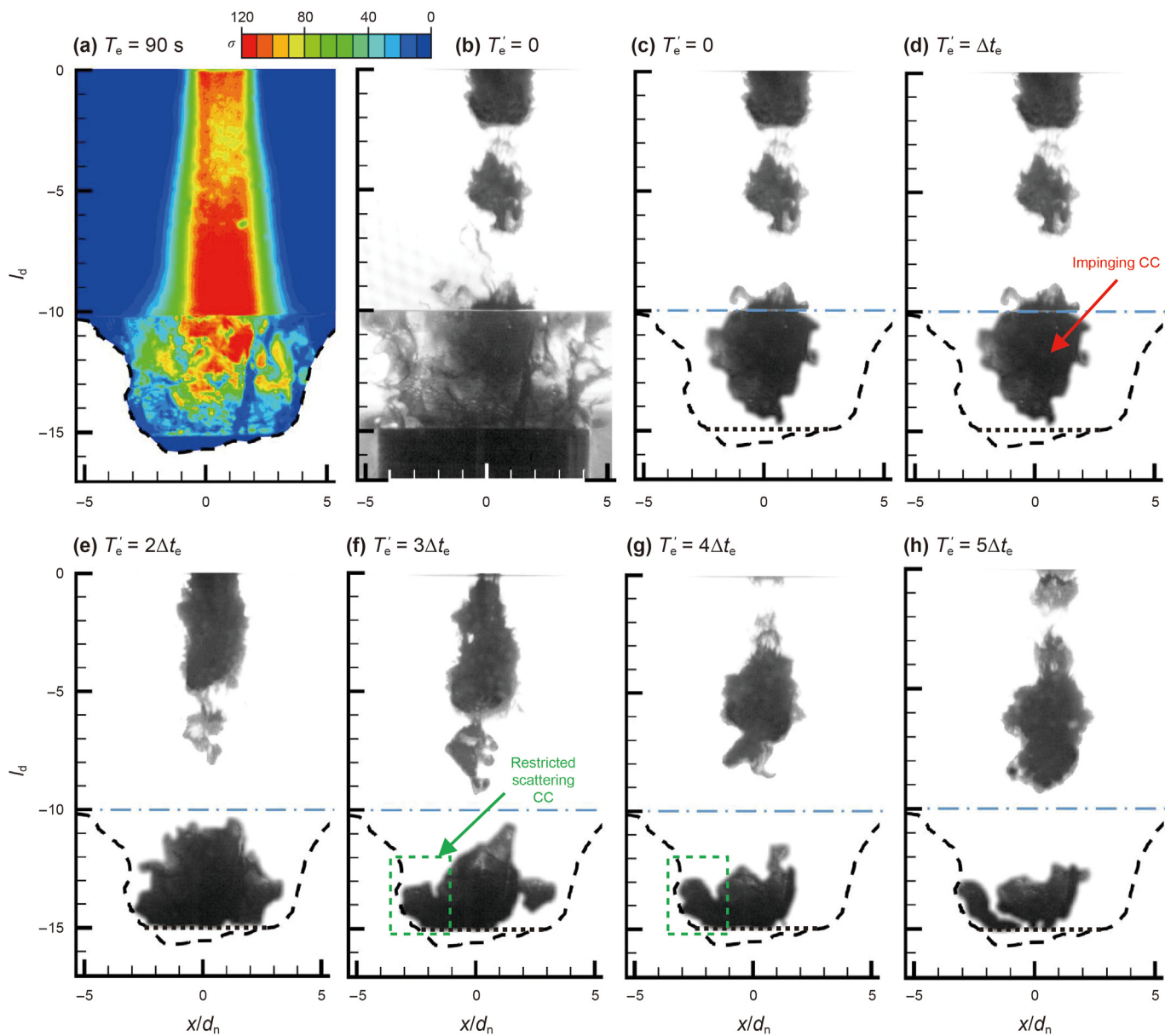


Fig. 15. (a) Standard deviation of the cavitation clouds at $l_2 = 10$ for the erosion at $T_e = 90$ s. (b) Original instantaneous photographs. (c)–(i) Instantaneous photographs.

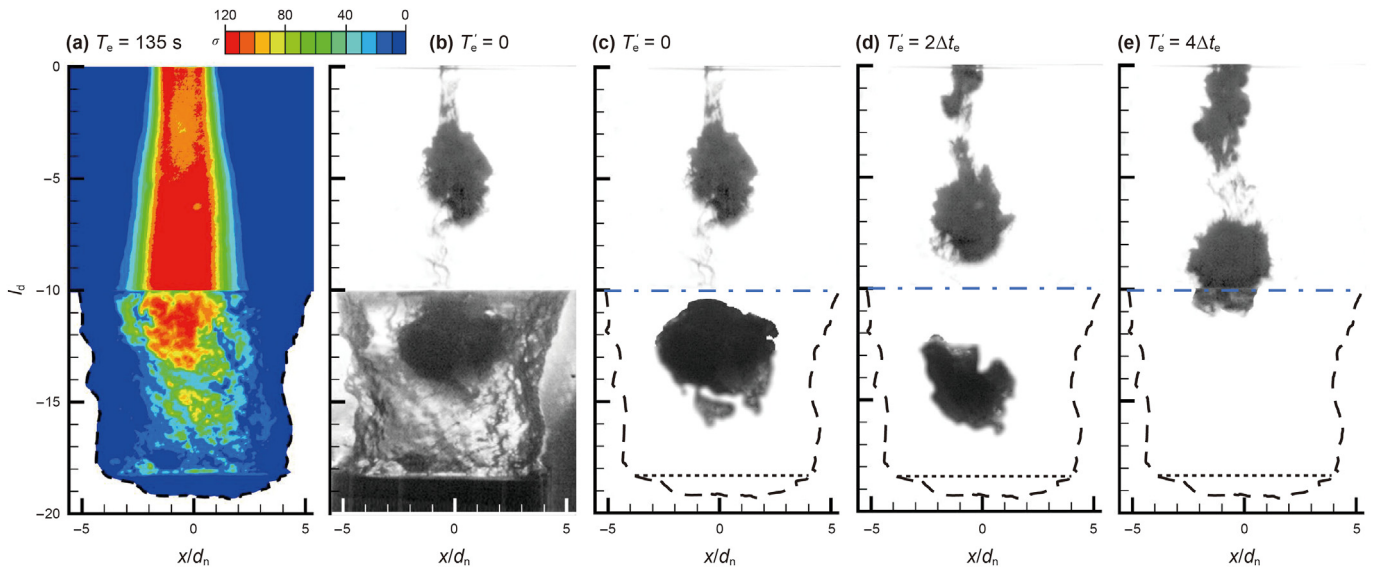


Fig. 16. (a) Standard deviation of the cavitation clouds at $l_2 = 10$ for the erosion at $T_e = 135$ s. (b) Original instantaneous photographs. (c)–(e) Instantaneous photographs.

erosion development, where the proper standoff distance and the exposure period are the major factors in maintaining the high drilling and rock cutting efficiency of the cavitating jet.

Funding

This work has been funded by the National Key R&D Program of China (Grant No. 2021YFB3401500), Engineering research 2023-GCKY-001, the National Natural Science Foundation of China (Grant Nos. 52004018, 52304119).

CRediT authorship contribution statement

Qi-Heng Zhu: Writing – original draft, Methodology. **Fei Ma:** Validation. **Bo-Shen Liu:** Methodology. **Tian-Xu Luo:** Software. **Yan Pan:** Data curation.

Declaration of competing interest

The authors declare that they have no known competing financial interests or personal relationships that could have appeared to influence the work reported in this paper.

References

- Cai, T.F., Chamorro, L.P., Ma, F., Zhu, Q.H., Han, J., 2023. Acoustic modes of self-excited cavitating waterjets on rock erosion. *Phys. Fluids* 35, 063322. <https://doi.org/10.1063/5.0153548>.
- Chahine, G.L., Hsiao, C., 2015. Modelling cavitation erosion using fluid – material interaction simulations. *Interface Focus* 5, 20150016. <https://doi.org/10.1098/rsfs.2015.0016>.
- Chen, Y., Fang, Z.L., Xiong, T., Hou, W.J., Zhang, Z.L., Shi, R.C., 2023. An experimental study on the erosion of sandstone by self-excited oscillation cavitating waterjet in submerged environment. *Ocean Eng.* 279, 114546. <https://doi.org/10.1016/j.oceaneng.2023.114546>.
- Chi, P., Zhang, S.L., Fu, J.H., Li, Q.F., Su, Y., Chang, H., Chen, Y.X., Yang, Y., 2022. Erosion experiments of shale using a cavitation jet. *Ocean Eng.* 261, 112115. <https://doi.org/10.1016/j.oceaneng.2022.112115>.
- Choi, J., Jayaprakash, A., Chahine, G.L., 2012. Scaling of cavitation erosion progression with cavitation intensity and cavitation source. *Wear* 278–279, 53–61. <https://doi.org/10.1016/j.wear.2012.01.008>.
- Crow, S.C., 1973. A theory of hydraulic rock cutting. *Int. J. Rock Mech. Min. Sci. Geomech. Abstracts* 10, 567–584. [https://doi.org/10.1016/0148-9062\(73\)90006-5](https://doi.org/10.1016/0148-9062(73)90006-5).
- Fan, C.X., Zhang, H.T., Kang, Y., Shi, H.Q., Li, D., 2023. Rock breaking performance of the newly proposed unsubmerged cavitating abrasive waterjet. *Int. J. Min. Sci. Technol.* 33, 843–853. <https://doi.org/10.1016/j.ijmst.2023.04.003>.

- Forman, S., Secor, G., 1974. The mechanics of rock failure due to water jet impingement. *Soc. Petrol. Eng. J.* 14, 10–18. <https://doi.org/10.2118/4247-pa>.
- Gavaises, M., 2008. Flow in valve covered orifice nozzles with cylindrical and tapered holes and link to cavitation erosion and engine exhaust emissions. *Int. J. Engine Res.* 9, 435–447. <https://doi.org/10.1243/14680874JER01708>.
- Ge, Z.L., Cao, S.R., Lu, Y.Y., Gao, F.F., 2022. Fracture mechanism and damage characteristics of coal subjected to a water jet under different triaxial stress conditions. *J. Petrol. Sci. Eng.* 208, 109157. <https://doi.org/10.1016/j.petrol.2021.109157>.
- Ge, Z.L., Lu, Y.Y., Tang, J.R., Hu, K., Zhang, W., 2011. Experimental study of mechanism of rock breakage with high-pressure cavitating water jets. *Advances in Civil Engineering and Architecture*. Trans Tech Publications Ltd., pp. 2130–2137. <https://doi.org/10.4028/www.scientific.net/amr.243-249.2130>.
- Jasper, S., Gradzki, D.P., Bracke, R., Hussong, J., Petermann, M., Lindken, R., 2021. Nozzle cavitation and rock erosion experiments reveal insight into the jet drilling process. *Chem. Ing. Tech.* 93, 1610–1618. <https://doi.org/10.1002/cite.202100056>.
- Jiang, T.W., Huang, Z.W., Li, J.B., Zhou, Y.S., Xiong, C., 2022. Experimental investigation of internal and external flow fields of jetting nozzles with different structures. *J. Petrol. Sci. Eng.* 217, 110891. <https://doi.org/10.1016/j.petrol.2022.110891>.
- Kang, C., Liu, H.X., Soyama, H., 2018. Estimation of aggressive intensity of a cavitating jet with multiple experimental methods. *Wear* 394–395, 176–186. <https://doi.org/10.1016/j.wear.2017.11.001>.
- Kang, Y.Q., Yang, R.S., Yang, L.Y., Li, C.X., Chen, J., Zhu, H.N., Liu, N., 2023. Theoretical and numerical studies of rock breaking mechanism by double disc cutters. *Int. J. Min. Sci. Technol.* 33, 815–828. <https://doi.org/10.1016/j.ijmst.2023.03.006>.
- Li, G.S., Huang, Z.W., Tian, S.C., Shen, Z.H., 2010. Research and application of water jet technology in well completion and stimulation in China. *Petrol. Sci.* 7, 239–244. <https://doi.org/10.1007/s12182-010-0009-9>.
- Li, G.S., Shen, Z.H., 2005. Advances in researches and applications of water jet theory in petroleum engineering. *Petrol. Explor. Dev.* 32, 96–99.
- Liu, B.S., Gao, Y., Ma, F., 2022. Aggressive ability improvement of self-resonating cavitating jets with double-hole nozzle. *J. Petrol. Sci. Eng.* 214, 110476. <https://doi.org/10.1016/j.petrol.2022.110476>.
- Liu, B.S., Ma, F., 2021. Erosion behavior of aluminum by an inclined cavitating jet. *Wear* 474–475, 203751. <https://doi.org/10.1016/j.wear.2021.203751>.
- Liu, B.S., Pan, Y., Ma, F., 2020. Pulse pressure loading and erosion pattern of cavitating jet. *Eng. Appl. Comput. Fluid Mech.* 14, 136–150. <https://doi.org/10.1080/19942060.2019.1695675>.
- Lu, Y.Y., Ge, Z.L., Yang, F., Xia, B.W., Tang, J.R., 2017. Progress on the hydraulic measures for grid slotting and fracturing to enhance coal seam permeability. *Int. J. Min. Sci. Technol.* 27, 867–871. <https://doi.org/10.1016/j.ijmst.2017.07.011>.
- Mitroglou, N., McLorn, M., Gavaises, M., Soteriou, C., Winterbourne, M., 2014. Instantaneous and ensemble average cavitation structures in diesel micro-channel flow orifices. *Fuel* 116, 736–742. <https://doi.org/10.1016/j.fuel.2013.08.060>.
- Momma, T., Lichtarowicz, A., 1995. A study of pressures and erosion produced by collapsing cavitation. *Wear* 186, 425–436. [https://doi.org/10.1016/0043-1648\(95\)07144-x](https://doi.org/10.1016/0043-1648(95)07144-x).
- Peng, C., Tian, S.C., Li, G.S., 2018. Joint experiments of cavitation jet: high-speed visualization and erosion test. *Ocean Eng.* 149, 1–13. <https://doi.org/10.1016/j.oceaneng.2017.11.009>.

- Sato, K., Sugimoto, Y., Ohjimi, S., 2009. Pressure-wave formation and collapses of cavitation clouds impinging on solid wall in a submerged water jet. *Proceedings of the 7th International Symposium on Cavitation*. August 17–22, Ann Arbor, MI.
- Soyama, H., 2017. Key factors and applications of cavitation peening. *Int. J. Peen. Sci. Technol.* 1, 3–60.
- Soyama, H., Sekine, Y., Saito, K., 2011. Evaluation of the enhanced cavitation impact energy using a pvdf transducer with an acrylic resin backing. *Measurement* 44, 1279–1283. <https://doi.org/10.1016/j.measurement.2011.03.027>.
- Soyama, H., Yamauchi, Y., Adachi, Y., Sato, K., Shindo, T., Oba, R., 1995. High-speed observations of the cavitation cloud around a high-speed submerged water jet. *JSME Int. J. Ser. B Fluids Therm. Eng.* 38, 245–251. <https://doi.org/10.1299/jsmeb.38.245>.
- Tomita, Y., Shima, A., 1986. Mechanisms of impulsive pressure generation and damage pit formation by bubble collapse. *J. Fluid Mech.* 169, 535–564. <https://doi.org/10.1017/s0022112086000745>.
- Wu, X.Y., Zhang, Y.Q., Hui, C.Y., Huang, H.C., Hu, Z.W., Li, G.S., Tian, S.C., 2023a. Cavitation damage inducing the improvement of jet breaking efficiency during hydrate drilling. *Ocean Eng.* 280, 114946. <https://doi.org/10.2139/ssrn.4331207>.
- Wu, X.Y., Zhang, Y.Q., Tan, Y.W., Li, G.S., Peng, K.W., Zhang, B., 2022. Flow-visualization and numerical investigation on the optimum design of cavitating jet nozzle. *Petrol. Sci.* 19, 2284–2296. <https://doi.org/10.1016/j.petsci.2022.05.016>.
- Wu, X.Y., Zhang, Y.Q., Xu, Z.Q., Zhao, S., Li, G.S., Tian, S.C., Tan, Y.W., Peng, K.W., 2023b. Structure optimization of the organ-pipe cavitating nozzle and its erosion ability test on hydrate-bearing sediments. *Petrol. Sci.* 20, 1104–1118. <https://doi.org/10.1016/j.petsci.2022.10.010>.
- Yamaguchi, A., Shimizu, S., 1987. Erosion due to impingement of cavitating jet. *J. Fluid Eng.* 109, 442–447. <https://doi.org/10.1115/1.3242686>.
- Yamauchi, Y., Soyama, H., Adachi, Y., Sato, K., Shindo, T., Oba, R., Oshima, R., Yamabe, M., 1995. Suitable region of high-speed submerged water jets for cutting and peening. *JSME Int. J. Ser. B Fluids Therm. Eng.* 38, 31–38. [https://doi.org/10.1016/s0301-9322\(97\)88469-8](https://doi.org/10.1016/s0301-9322(97)88469-8).